

# The Advanced LIGO Input Optics

Chris L. Mueller,<sup>1, a)</sup> Muzammil A. Arain,<sup>1, b)</sup> Giacomo Ciani,<sup>1</sup> Ryan. T. DeRosa,<sup>2</sup> Anamaria Effler,<sup>2</sup> David Feldbaum,<sup>1</sup> Valery V. Frolov,<sup>3</sup> Paul Fulda,<sup>1</sup> Joseph Gleason,<sup>1, c)</sup> Matthew Heintze,<sup>1</sup> Eleanor J. King,<sup>4</sup> Keiko Kokeyama,<sup>2</sup> William Z. Korth,<sup>5</sup> Rodica M. Martin,<sup>1, d)</sup> Adam Mullavey,<sup>3</sup> Jan Poeld,<sup>6</sup> Volker Quetschke,<sup>7</sup> David H. Reitze,<sup>1, e)</sup> David B. Tanner,<sup>1</sup> Luke F. Williams,<sup>1</sup> and Guido Mueller<sup>1</sup>

<sup>1)</sup> *University of Florida, Gainesville, FL 32611, USA*

<sup>2)</sup> *Louisiana State University, Baton Rouge, LA 70803, USA*

<sup>3)</sup> *LIGO Livingston Observatory, Livingston, LA 70754, USA*

<sup>4)</sup> *University of Adelaide, Adelaide, SA 5005, Australia*

<sup>5)</sup> *LIGO, California Institute of Technology, Pasadena, CA 91125, USA*

<sup>6)</sup> *Max-Planck-Institut für Gravitationsphysik, 30167 Hannover, Germany*

<sup>7)</sup> *University of Texas at Brownsville, Brownsville, TX 78520, USA*

(Dated: February 4, 2022)

The Advanced LIGO gravitational wave detectors are nearing their design sensitivity and should begin taking meaningful astrophysical data in the fall of 2015. These resonant optical interferometers will have unprecedented sensitivity to the strains caused by passing gravitational waves. The input optics play a significant part in allowing these devices to reach such sensitivities.

Residing between the pre-stabilized laser and the main interferometer, the input optics is tasked with preparing the laser beam for interferometry at the sub-attometer level while operating at continuous wave input power levels ranging from 100 mW to 150 W. These extreme operating conditions required every major component to be custom designed. These designs draw heavily on the experience and understanding gained during the operation of Initial LIGO and Enhanced LIGO. In this article we report on how the components of the input optics were designed to meet their stringent requirements and present measurements showing how well they have lived up to their design.

## I. INTRODUCTION

A worldwide effort to directly detect gravitational radiation in the 10 Hz to a few kHz frequency range with large scale laser interferometers has been underway for the past two decades. In the United States the Laser Interferometer Gravitational-Wave Observatories (LIGO) in Livingston, LA (LLO) and in Hanford, WA, (LHO) have been operating since the early 2000's. Initial and enhanced LIGO produced several significant upper limits, but did not have the sensitivity to make the first direct detection of gravitational waves. During this time of operation a significant amount of effort was invested by the LIGO Scientific Collaboration to research and design Advanced LIGO (aLIGO), the first major upgrade of initial LIGO. In 2011 the initial LIGO detectors were decommissioned and installation of these upgrades started. The installation was completed in 2014 and the commissioning phase has begun for many of the upgraded subsystems at the LIGO ob-

servatories. This paper focuses on the input optics of aLIGO.

The main task of the input optics (IO) subsystem is to take the laser beam from the pre-stabilized laser system<sup>1</sup> (PSL) and prepare and inject it into the main interferometer (IFO). The PSL consists of a master laser, an amplifier stage, and a 200W slave laser which is injection-locked to the amplified master laser. The 200W output beam is filtered by a short optical ring cavity, the pre-mode cleaner, before it is turned over to the IO (see Figure 1). The PSL pre-stabilizes the laser frequency to a fixed spacer reference cavity using a tunable sideband locking technique. The PSL also provides interfaces to further stabilize its frequency and power.

The IFO is a dual-recycled, cavity-enhanced Michelson interferometer<sup>2</sup> as sketched in Figure 2. The field enters the 55 m folded power recycling cavity (PRC) through the power recycling mirror (PRM). Two additional mirrors (PR2, PR3) within the PRC form a fairly fast telescope to increase the beam size from  $\sim 2$  mm to  $\sim 50$  mm (Gaussian beam radius) before the large beam is split at the beam splitter (BS) and injected into the two 4 km arm cavities formed by the input and end test masses. The reflected fields recombine at the BS and send most of the light back to the PRM where it constructively interferes with the injected field<sup>3</sup>. This leads to a power enhancement inside the power recycling cav-

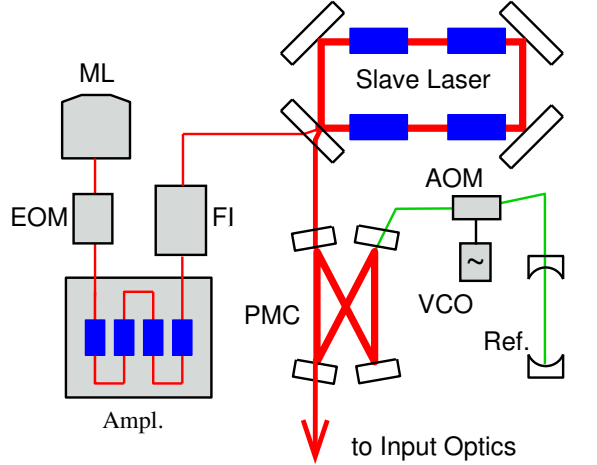
<sup>a)</sup>Electronic mail: cmueller@phys.ufl.edu

<sup>b)</sup>Present Address: KLA-Tencor, Milpitas, CA 95035, USA

<sup>c)</sup>Present Address: [Get Current Address 1](#)

<sup>d)</sup>Present Address: [Get Current Address 2](#)

<sup>e)</sup>Present Address: LIGO Laboratory, California Institute of Technology, Pasadena, CA 91125, USA



ML: Master Laser  
 EOM: Electro-optic modulator  
 AOM: Acousto-optic modulator  
 VCO: Voltage Controlled Osc.  
 FI: Faraday Isolator  
 Ref.: Reference Cavity  
 PMC: Pre-mode cleaner  
 Ampl.: Amplifier

Figure 1. Sketch of the pre-stabilized laser (PSL) system. Red: Main beam, Green: Pick-off beam. The figure shows the low power master laser, the phase-correcting EOM, the amplifier stage, a high power Faraday isolator, and the high power slave laser. The pre-mode cleaner suppresses higher order spatial modes of the laser beam. The VCO drives the AOM which shifts the frequency of the pick-off beam to stabilize the sideband and with it the frequency of the laser to the reference cavity.

ity and provides additional spatial, frequency, and amplitude filtering of the laser beam. The second output of the BS sends light into the 55 m long folded signal recycling cavity<sup>4</sup> (SRC) which also consists of a beam reducing telescope (SR2, SR3) and the semi-transparent signal recycling mirror (SRM).

This paper is organized as follows: Section II gives an overview of the IO; its functions, components, and the general layout. Section III discusses the requirements for the IO. Section IV presents the core of this paper; it will describe individual IO components, their performance in pre-installation tests and the detailed layout of the IO. Section V discusses the expected and measured in-vacuum performance as known by the time of writing. The final integrated testing of the IO subsystem at design sensitivity requires the main interferometer to be nearly fully commissioned to act as a reference for many of the required measurements; this will be discussed in Section VI.

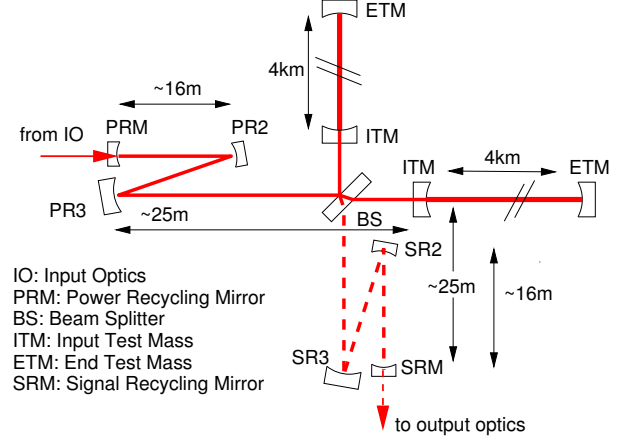


Figure 2. Sketch of the main interferometer which consists of two 4 km arm cavities, the beam splitter, and the folded 55 m long power and signal recycling cavities. The input optics is located between this system and the PSL shown in Figure 1.

## II. OVERVIEW OF THE INPUT OPTICS

Figure 3 shows a sketch of the first part of the input optics. This part is co-located with the PSL on the same optical table inside the laser enclosure, outside of the vacuum system. It prepares the laser beam for the injection into the vacuum system. The beam from the PSL is first routed through a half wave plate and a polarizing beam splitter. These two elements form a manual power control stage which is used mainly during alignment processes on the optical table. The following mirror transmits 2.5% of the light. This light is used by the arm length stabilization (ALS) system during lock acquisition of the main interferometer<sup>5</sup>.

Most of the light is sent through an electro-optic modulator (EOM) which modulates the phase of the laser field with three different modulation frequencies. Two of these frequencies are used by the interferometer sensing and control system (ISC) to sense most of the longitudinal and alignment degrees of freedom of the mirrors inside the IFO and to stabilize the laser frequency and the alignment of the laser beam into the interferometer. The third frequency is used to control the input mode cleaner (IMC). The two lenses L1 and L2 mode match the beam to the in-vacuum input mode cleaner. The next steering mirror directs the beam through another half wave plate inside a motorized rotation stage in front of two thin film polarizers. This second power control stage is used during operations to adjust the power to the requested level. The periscope raises the height of the beam and steers it into the vacuum system. The top mirror is mounted on a piezo actuated mirror

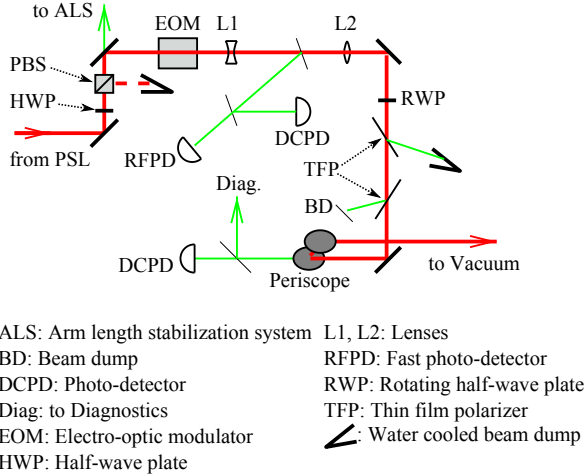


Figure 3. The IO on the PSL modulates the phase of the laser beam with the EOM, mode matches the light into the input mode cleaner (located inside the vacuum system), and controls the power injected into vacuum system.

mount to fine tune the alignment of the beam into the vacuum chamber.

Between the lenses is a wedge to pick off a small fraction of the laser beam for diagnostic purposes. A fast photo detector monitors the residual amplitude modulation at the phase modulation frequencies while a second photodetector monitors the DC power. A fraction of the main beam also transmits through the bottom periscope mirror and is used to monitor the power going into the vacuum system as well as the size, shape, and quality of the beam.

Following the periscope, the main beam is sent through a metal tube which includes a mechanical shutter and through HAM1<sup>6</sup> into HAM2; all in-vacuum IO components are mounted on seismically isolated optical tables inside HAM2 and HAM3. As shown in Figure 4, the beam passes over the FI to a second periscope which lowers the beam to the in-vacuum beam height. The next element in the IO is the suspended IMC, a 33 m long triangular cavity. The two flat input and output mirrors, named MC1 and MC3 respectively, are located in HAM2 while the third curved mirror, MC2, is located in HAM3. Following MC3 are two suspended mirrors, IM1 and IM2, which steer the beam through the FI. IM3 and IM4 are used to steer the beam into the PRC. IM2 and IM3 are curved to mode match the output mode of the IMC to the mode of the main interferometer.

Two of the steering mirrors, IM1 and IM4, transmit a small fraction of the light creating three different auxiliary beams which are used to monitor the power and spatial mode of the IMC transmitted beam, of the beam going into the IFO, and of

the beam which is reflected from the IFO. The latter two beams are routed to IOT2R<sup>7</sup>, an optical table on the right side of HAM2, while the first beam and the field which is reflected from MC1 are routed to IOT2L on the left side of HAM2. The position of the forward going beam through IM4 is monitored with an in-vacuum quadrant photo detector while a large fraction of this beam is also sent to an in-vacuum photo detector array which is used to monitor and stabilize the laser power before it is injected into the IFO. Most of the IFO reflected field goes back to the FI where it is separated from the incoming beam. This field is routed into HAM1 where it is detected to generate length and alignment sensing signals.

In HAM3, a small fraction of the intra-mode cleaner field transmits through MC2 onto a quadrant photo detector to monitor the beam position on MC2. The forward and backwards traveling waves inside the PRC partly transmit through PR2 and are routed into HAM1 and to an optical breadboard inside HAM3, respectively. These beams are used by ISC for sensing and control of the interferometer and for diagnostic purposes. The breadboard holds two lenses which image the beam with orthogonal Gouy phases onto two quadrant photo detectors to monitor beam position and pointing inside the power recycling cavity. IOT2R and IOT2L host photo detectors and digital cameras to monitor the power and beam sizes in each of the picked-off beams. IOT2L also hosts the photo detectors which are used by the interferometer sensing and control system to generate length and alignment sensing signals for the input mode cleaner.

While the figure shows all key components in the correct sequence, we intentionally left out the detailed beam routing, the baffles used to protect all components from the laser beam in case of misalignments, and the beam dumps to capture all ghost beams.

A complete document tree which contains all design and as-built layouts as well as drawings of all components is available within the LIGO Document Control Center<sup>8</sup> (DCC) under document number E1201013<sup>9</sup>.

### III. INPUT OPTICS REQUIREMENTS

The aLIGO interferometer can be operated in different modes to optimize the sensitivity for different sources<sup>10</sup>. These modes are characterized by the input power and the microscopic position and reflectivity of the signal recycling mirror. The requirements for the aLIGO input optics are specified to simultaneously meet the requirements for all an-

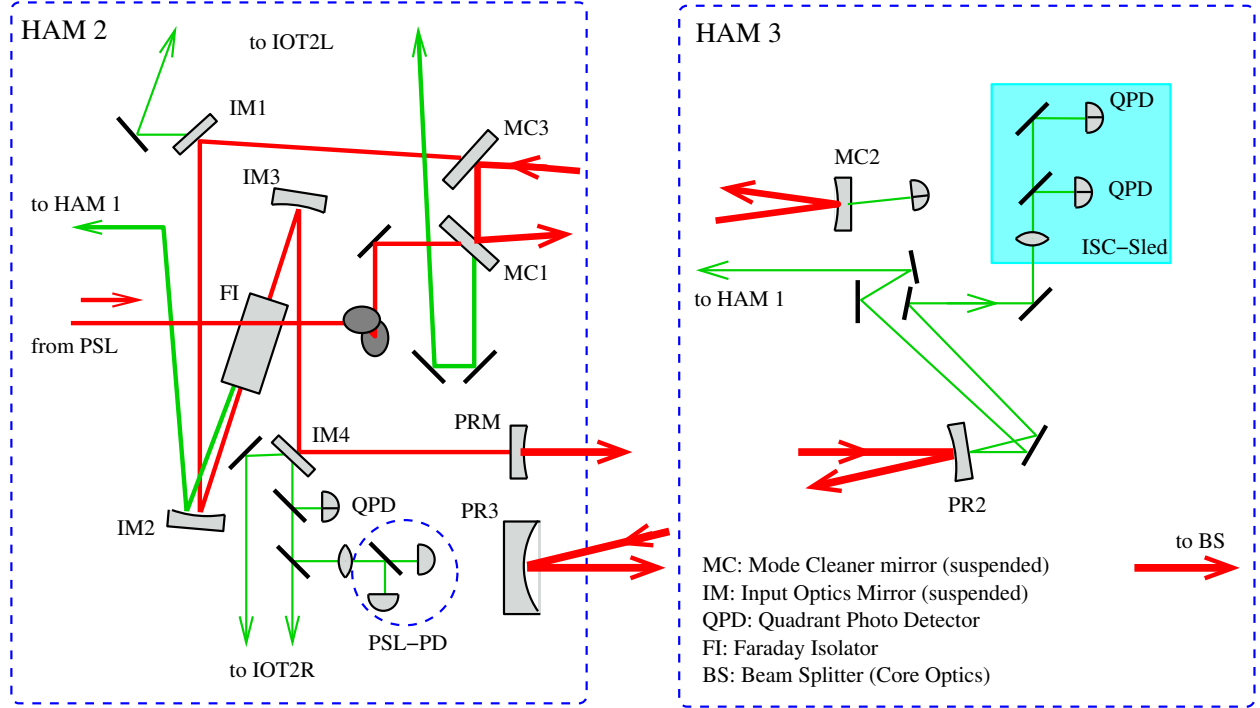


Figure 4. A sketch of the in-vacuum components and beam directions within the input optics in HAM 2 and HAM 3. The red beam is the forward going main beam while the green beams are auxiliary beams. The main items in the in-vacuum input optics are the input mode cleaner (IMC) which is formed by the three mirrors MC1, MC2, MC3; the Faraday isolator (FI); and the four suspended steering mirrors IM1-4 of which IM2 and 3 match the spatial mode of the IMC into the main interferometer. The recycling cavity mirrors PRM, PR2, and PR3 are not part of the input optics. The ISC sled in HAM3 belongs to the interferometer sensing and control subsystem and provides alignment signals for the recycling cavity.

anticipated science modes and address all degrees of freedom of the laser field. Requirements in aLIGO are defined for three distinct frequency ranges: DC, the control band up to 10 Hz, and the signal or detection band from 10 Hz to a few kHz. The requirements in the detection band are defined in terms of linear spectral densities and include a safety factor of ten for all technical noise sources. To first order, a perfectly symmetric Michelson interferometer is insensitive to all input noise sources which is an often overlooked reason for its use in the first place. However, all degrees of freedom of the injected laser field couple via some asymmetry to the output signal. This drives the requirements in the control band which are usually defined as RMS values. The more critical requirements for the IO are:

**Power:** The high power science modes require to inject 125 W of mode matched light into the interferometer with less than an additional 5% in higher order modes. The PSL has to deliver 165 W of light in an appropriate TEM<sub>00</sub> mode. Consequently, the net efficiency of TEM<sub>00</sub> optical power transmission from the PSL output to the main interferometer has to be above 75%. This sets limits on accumulated losses

in all optical components but also limits the allowed thermal lensing in the EOM, the FI, and the power control stages; the reflective optics and fused silica lenses are much less susceptible to thermal lensing. Efficient power coupling is also dependent on good mode matching between the recycling cavities and the arm cavities in the main interferometer.

**Power Control:** The injected power into the interferometer has to be adjustable from the control room from minimum to full power for diagnostic and operational purposes, to acquire lock of the main interferometer, and to operate between different science modes. The rate of power change ( $dP/dt$ ) has to be sufficiently small to limit the radiation pressure kick inside the IMC and the main interferometer to a level that can be handled by the length and alignment control system. It has to be sufficiently fast to not limit the time to transition to full power after lock acquisition; i.e. it should be possible to change from minimum to maximum power within a few seconds.

Note that minimum power here can not mean zero power because of the limited extinction ratio of polarizers. Going to zero power requires actuation of

the aforementioned mechanical shutter which can only be accessed manually between the laser enclosure and HAM1. The emergency shutter is part of the PSL laser system and cuts the laser power at the source. Furthermore, the power control system within the IO is not used for actively stabilizing the laser power within the control or the detection band.

*Power fluctuations:* Fluctuations in the laser power can couple through many different channels to the error signal. The noise scales with the asymmetries in the interferometer. Two different mechanisms are expected to dominate the susceptibility of the interferometer to power fluctuations. The optical power inside the arm cavities will push the test masses outwards. Any change in power will cause fluctuations in that pressure which can lead to displacement noise at low frequencies. The susceptibility to radiation pressure noise scales with differences in the power build up inside the arm cavities and it is assumed that these differences are below 1%. At high frequencies, the signal itself limits the allowed power fluctuations. In lock the two arm cavities are detuned by a few pm which causes some light to leak out to the dark port<sup>11</sup>. Gravitational waves will modulate these offsets causing the light power to fluctuate. Obviously, power fluctuations in the laser itself, although highly filtered by the interferometer, will cause similar fluctuations. The relative intensity noise in the detection band has to be below  $2 \times 10^{-9}/\sqrt{\text{Hz}}$  at 10 Hz increasing with  $f$  to  $2 \times 10^{-8}/\sqrt{\text{Hz}}$  at 1 kHz and remaining flat after this<sup>12</sup>. Furthermore, the expected seismically excited motion of the test masses limits the allowed radiation pressure noise in the control band to  $10^{-2}/\sqrt{\text{Hz}}$  below 0.2 Hz. Above 0.2 Hz, the requirements follow two power laws; initially  $f^{-7}$  then  $f^{-3}$ , before connecting with the detection band requirement at 10 Hz.

The IO does not provide any active element to change or stabilize the laser power within the control or the detection band. The PSL uses a first loop which stabilizes the laser power measured with a photo-detector on the PSL table to  $2 \times 10^{-8}/\sqrt{\text{Hz}}$  between 20 and 100 Hz and meeting the aforementioned requirements above 100 Hz. The PSL also measures the power of the injected field with the photo detector array shown (PSL-PD) in Figure 4. The IO has to supply this auxiliary beam and maintain a sufficiently high correlation with the injected beam and minimize the chances of additional power fluctuations within any of these two beams.

*Frequency fluctuations:* In the detection band, the laser frequency will ultimately be stabilized to the common mode of the two arm cavities which are the most stable references available in this frequency range. At lower frequencies the arm cavi-

ties are not a good reference and are made to follow the frequency reference inside of the PSL. The input mode cleaner acts as a frequency reference during lock acquisition and as an intermediate frequency reference during science mode. It is integrated into the complex and nested laser frequency stabilization system. Based on the expected common mode servo gain the frequency noise requirements for the IMC are set to:

$$\begin{aligned}\delta\nu(f = 10 \text{ Hz}) &< 50 \frac{\text{mHz}}{\sqrt{\text{Hz}}} \\ \delta\nu(f \geq 100 \text{ Hz}) &< 1 \frac{\text{mHz}}{\sqrt{\text{Hz}}}.\end{aligned}$$

These requirements can be expressed equivalently as length fluctuations of the IMC:

$$\begin{aligned}\delta\ell(f = 10 \text{ Hz}) &< 3 \cdot 10^{-15} \frac{\text{m}}{\sqrt{\text{Hz}}} \\ \delta\ell(f \geq 100 \text{ Hz}) &< 6 \cdot 10^{-17} \frac{\text{m}}{\sqrt{\text{Hz}}}.\end{aligned}$$

*RF modulation frequencies:* The main laser field consists of a carrier and multiple pairs of sidebands. The carrier has to be resonant in the arm cavities and the power recycling cavity; the resonance condition in the signal recycling cavity depends on the tuning and specific science mode. One pair of sidebands must be resonant in the power recycling cavity while the second pair must resonate in both the power and signal recycling cavity. The modulation signals of  $f_1 = 9.1 \text{ MHz}$  and  $f_2 = 45.5 \text{ MHz}$  are provided by the interferometer sensing and control system. A third modulation frequency of  $f_3 = 24.1 \text{ MHz}$  is required to sense and control the input mode cleaner. The last pair of sidebands should be rejected by the input mode cleaner so as not to interfere with the sensing and control system of the main interferometer.

*RF modulation depth:* The required modulation depths depend on the final length and alignment sensing and control scheme. This scheme is likely to evolve over the commissioning time but the current assumption is that a modulation index of 0.4 for a 24dBm signal driving the EOM is more than sufficient. Note that this only applies to the two modulation frequencies which are used for sensing and control of the main interferometer; the modulation index for the third frequency need only be large enough to control the IMC.

The classic phase modulation/demodulation sensing scheme for a single optical cavity measures how much the cavity converts phase modulation into amplitude modulation when near resonance. Unfortunately all phase modulators also modulate the amplitude of the laser field. This amplitude modulation

can saturate the RF amplifiers and mixers in the detection chain and generate offsets in the error signals which have to be compensated. aLIGO requires that the amplitude modulation index is less than  $10^{-4}$  of the phase modulation index.<sup>13</sup>

*RF modulation noise:* Changes in the amplitude and phase of the RF modulation signals can change the dark port signal by changing the power build-up of the carrier in the arm cavities or through cross coupling in the length and alignment sensing and control schemes. These effects were analyzed by the ISC group<sup>10</sup>. The analysis uses specifications from a commercial crystal oscillator manufacturer as the expected oscillator phase and amplitude noise. These specifications for phase noise are  $10^{-5}\text{rad}/\sqrt{\text{Hz}}$  at 10 Hz falling with  $1/f^{3/2}$  to  $3 \times 10^{-7}\text{rad}/\sqrt{\text{Hz}}$  at 100 Hz and then a little faster than  $1/f$  to  $2 \times 10^{-8}\text{rad}/\sqrt{\text{Hz}}$  at a kHz above which the requirement stays constant. The specifications for amplitude noise are  $10^{-7}/\sqrt{\text{Hz}}$  at 10 Hz falling with  $1/f$  between 10 and 100 Hz and then with  $1/\sqrt{f}$  until 1 kHz above which it stays constant at  $3 \times 10^{-9}/\sqrt{\text{Hz}}$ . These specifications have been adopted as requirements although the analysis shows that they could be relaxed at higher frequencies.

*Beam jitter:* Changes in the location and direction of the injected beam can be described as scattering light from the  $\text{TEM}_{00}$  into a  $\text{TEM}_{10}$  mode. This light scatters back into the  $\text{TEM}_{00}$  mode inside a misaligned interferometer and creates noise in the gravitational wave signal.<sup>14</sup> This is an example where noise in the detection band, here beam jitter, couples to noise in the control band, here tilt of the input test masses. It is expected that the test masses will all be aligned to better than 2 nrad RMS with respect to the nominal optical axis of the interferometer. Under this assumption, the relative amplitude of the injected 10-mode has to stay below  $10^{-6}/\sqrt{\text{Hz}}$  at 10 Hz falling with  $1/f^2$  until 100 Hz above which the requirement stays constant at  $10^{-8}/\sqrt{\text{Hz}}$ .

*Optical isolation:* The FI isolates the IMC from back reflected light from the main interferometer. The requirements for the isolation ratio are based on experience gained during the initial years of operating LIGO and also VIRGO. Virgo operated for a long time without a FI between the mode cleaner and the main interferometer and encountered problems due to the uncontrolled length between the IMC and IFO<sup>15</sup> (a parasitic interferometer). Initial and enhanced LIGO never encountered any major problems with insufficient optical isolation in the FI. The requirements of 30dB for the optical isolation in the FI were set based on the experience in initial LIGO, taking into account the higher injected power.

*Additional requirements:* It is well known that parasitic interferometers and scattered light together with mechanically excited surfaces can add frequency and amplitude noise to a laser beam. The IO adopted a policy to limit the added noise to 10% of the allowed noise; note that the allowed frequency and amplitude noise prior to the input mode cleaner is significantly higher than after the mode cleaner. This drives requirements on the residual motion of the optical components, the surface quality of all optical components and their coatings, and on the placement and efficiency of the optical baffles. The requirement to align the IO drives requirements on actuation ranges for all optics and, last but not least, the IO has to meet the stringent cleanliness and vacuum requirements of aLIGO. These requirements are discussed throughout the paper when relevant.

The official requirements were originally captured in LIGO document T020020<sup>16</sup> and have been derived, updated and clarified in several other documents which are all available under E1201013.<sup>9</sup>

#### IV. INPUT OPTICS COMPONENTS AND FINAL LAYOUT

This section will first discuss the individual components and their measured performance. This will be followed by a description of the optical layout which includes a discussion of beam parameters and mode matching between the various areas.

##### A. Electro-optic modulators

The EOM must use a material capable of withstanding CW optical powers of up to 200 W and intensities up to  $25\text{ kW}/\text{cm}^2$ . At these power levels the induced thermal lensing, stress induced depolarization, and damage threshold of the electro-optic material must be taken into consideration. Rubidium titanyl phosphate (RTP) was chosen many years ago over other electro-optic materials, such as rubidium titanyl arsenate ( $\text{RbTiOAsO}_4$  or RTA) and lithium niobate ( $\text{LiNbO}_3$ ), as the most promising modulator material after a literature survey, discussions with various vendors, and corroborating lab experiments.<sup>17,18</sup> RTP has a very high damage threshold, low optical absorption, and a fairly high electro-optical coefficient. Enhanced LIGO (eLIGO) allowed for testing of the material and design over a one-year period at 30 W input power.<sup>19</sup>

The aLIGO EOM uses a patented design<sup>20</sup> which is very similar to the one used in eLIGO; both consist of a  $4 \times 4 \times 40\text{ mm}$  long wedged RTP crystal (see Figure 5). The  $2.85^\circ$  wedges prohibit parasitic



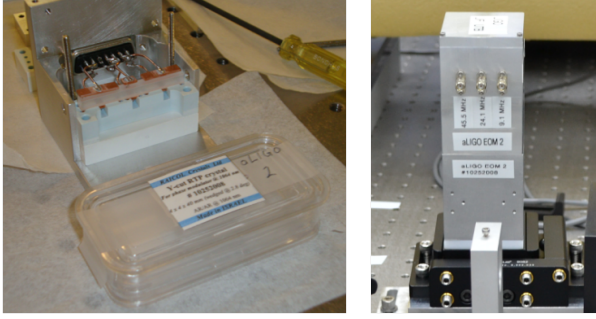


Figure 5. Images of the EOM. The housing uses two modules; the crystal and the electrodes are placed in the lower module while the upper module houses the coils for the three resonant circuits. The left picture shows the inside of the lower module: the aLIGO EOM consists of a wedged RTP crystal with three pairs of electrodes. The two 15 mm electrodes on the outside are used for the main modulation frequencies  $f_1 = 9.1$  MHz and  $f_2 = 45.5$  MHz. The 7 mm electrodes in the middle are used for  $f_3 = 24.1$  MHz. The crystal and the electrodes are clamped between two macor pieces. The right picture shows the final modulator (both modules) on a five axis alignment stage.

interferometers from building up inside the crystal and allow for separation of the two polarizations of the injected laser field with an extinction ratio of better than  $10^5$ . This separation avoids polarization rotation which could otherwise convert phase modulation to amplitude modulation. The AR coated surfaces have a reflectivity of less than 0.1%. For aLIGO we use two 15 mm long pairs of electrodes for the two main modulation frequencies and one 7 mm long pair for the auxiliary frequency used to control the IMC. Each electrode pair forms a capacitor which is part of a resonant circuit in the form of a  $\pi$  network where the additional inductor and capacitor are used to simultaneously match the resonance frequency and create the required  $50\ \Omega$  input impedance.

After installation and alignment at both sites, initial tests confirmed that the RTP crystals do not produce a significant thermal lens. An optical spectrum analyzer was used to measure the modulation index as a function of modulation frequency for each of the three resonant circuits. The results are shown in Figure 6. The modulation indices for  $f_1$  and  $f_2$  meet the requirements at both sites while the  $f_3$  modulation index is still a little low, especially at LLO. However, early commissioning experience indicates that the modulation indices are sufficient for the aLIGO length and alignment sensing scheme and it was decided to use the EOM as is for now and potentially improve the resonant circuits later if necessary.

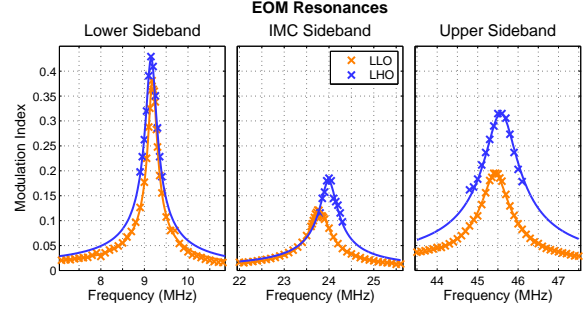


Figure 6. The measured modulation indices for both the Livingston and Hanford EOM with a 24 dBm drive. The data is shown together with a best fit to the expected circuit response.

The residual amplitude modulation (RFAM) produced by the EOM was also characterized. The AM/PM ratio for each of the three sidebands was measured to be  $1.0 \cdot 10^{-4}$ ,  $1.2 \cdot 10^{-5}$ , and  $4.1 \cdot 10^{-5}$  for the 9.1 MHz, 24.0 MHz and 45.5 MHz sidebands respectively. All three measurements come out to be at or below the requirement of  $10^{-4}$  derived by Kokeyama et. al.<sup>13</sup> The temperature dependence of the RFAM generation was briefly investigated and was found to be able to push the AM/PM ratio at 9.1 MHz up as high as  $3 \cdot 10^{-4}$ . This may need to be addressed with a temperature stabilization servo in the future if RFAM is found to be an issue during detector commissioning, but the design of the modulator was left unchanged until such an issue arises.

Detailed design drawings, assembly instructions, and test reports are available under LIGO document number T1300084.<sup>21</sup>

## B. Faraday isolator

The FI is a much more complicated optical device compared to the EOM. It is more susceptible to thermal lensing and its location after the mode cleaner amplifies the requirement to maintain a good spatial mode. The FI has to handle between 20 to 130 W of laser power without significantly altering the beam profile or polarization of the beam. Like the EOM, the aLIGO FI is also very similar to the FI used in eLIGO<sup>19</sup>. Both were designed to minimize and mitigate thermal lensing and thermal stress induced depolarization by compensating these effects in subsequent crystals<sup>22,23</sup>.

The aLIGO FI design consists of a Faraday rotator, a pair of calcite-wedge polarizers, an element with a negative  $dn/dT$  for thermal-lens compensation, and a picomotor-controlled half-wave plate for restoring the optical isolation in-situ. In addition, a

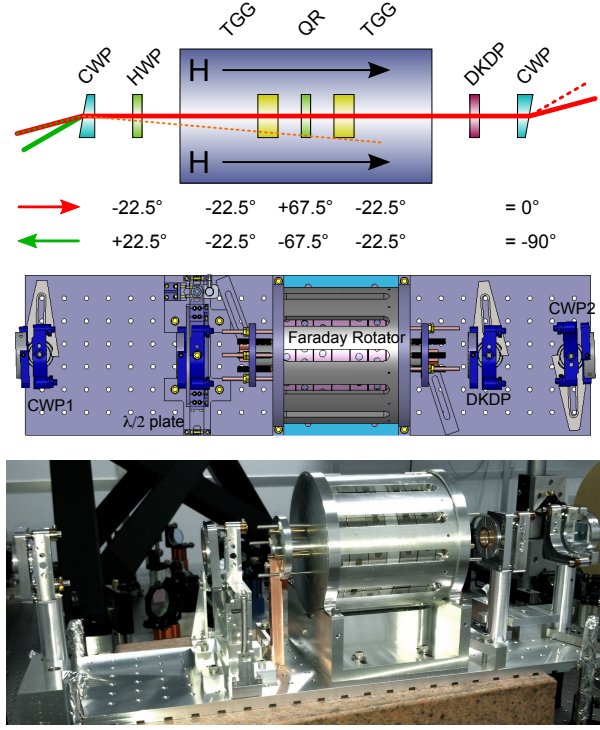


Figure 7. Advanced LIGO Faraday isolator (from top to bottom): optical layout, design, final product.

heat sink is connected to the holders of the magneto-optical crystals to drain excess heat into the FI breadboard. The Faraday rotator is based on an arrangement developed by Khazanov et. al.<sup>24</sup>, that uses a pair of  $\sim 1$  cm long Terbium Gallium Garnet (TGG) crystals as magneto-optical elements, each nominally producing a  $22.5^\circ$  rotation of the electric field when placed in a magnetic field of about 1T. They are separated by a  $\sim 1$  cm long piece of quartz that rotates the polarization field reciprocally by  $67.5^\circ \pm 0.6^\circ$ . This arrangement (shown schematically at the top of Figure 7) allows thermally induced birefringence produced in the first magneto-optical element to be mostly compensated in the second one. The HWP is a zero-order epoxy-free quartz half-wave plate. It is set to rotate the polarization by an additional  $22.5^\circ$  to have  $0^\circ$  net rotation in the forward going and  $90^\circ$  in the backward going direction.

All crystals were selected to minimize absorption, thermal beam distortion and surface roughness. Those made of harder and non-hygroscopic materials; the half-wave plate, quartz rotator, and TGG crystals, are all super-polished (surface roughness below 0.5 nm) and received a custom low loss IBS AR coating with a rest reflectivity of less than 300 ppm. The softer calcite polarizers and the

DKDP crystal were procured from the manufacturers with their standard polishings and coatings. The two calcite polarizers each have a thickness of  $\sim 5$  mm and are wedged at  $8.5^\circ$  to allow the orthogonally polarized beams to separate sufficiently. The calcite wedges have an extinction ratio of at least  $10^5$  and more than 99% optical efficiency.

The magnetic field is created by a stack of seven magnetized Fe-Nb magnetic disks<sup>25</sup> each having a bore of 24 mm and a thickness of 19.7 mm. This stack produces a maximum axial field of 1.16 T (LLO) and 1.55 T (LHO) near its center which falls off towards the end. The difference in the magnetic field is caused by the selection of the magnetic materials and the thermal treatment of the individual magnets.<sup>26</sup> The TGG crystals and quartz rotator are installed about 3 cm apart from each other before being fine tuned to produce  $22.5^\circ$  of rotation by adjusting their depth in the magnet. The entire FI is mounted on a 648 mm x 178 mm breadboard for convenient transfer into the HAM chamber after out-of-vacuum optimization.

After undergoing a thorough cleaning procedure, the FI was assembled and aligned with the main PS� beam in the laser enclosure. The optical table in the enclosure is made from stainless steel while the optical table in HAM2 is made from aluminum. The differences in magnetic susceptibility are significant enough to require the FI to be raised with an  $\sim 11$  cm thick granite block visible in the bottom picture in Figure 7. The bottom periscope mirror in Figure 3 was removed and the beam was sent via several mirrors through the FI. This setting ensured that the beam parameters, beam size and divergence angle, are very similar to the ones expected in-vacuum.

The thermal lensing of the FI was determined from beam-scan measurements of a sample of the beam after it was transmitted through the isolator for incident powers as high as 120 W at LLO and 140 W at LHO. At both sites, the diagnostic beam was focused with a lens of 1 m focal length and the beam profile was recorded with CCD or rotating slit beam scans as a function of power for different DKDP crystals. The thermal lens at the location of the FI was then computed using an ABCD matrix algorithm. Figure 8 shows the thermal lensing measurements for the TGG crystals and different DKDP crystals at LHO and LLO. The length of the DKDP crystal was chosen to compensate the a priori unknown thermal lensing in the TGG crystals. Based on experience from initial and enhanced LIGO, the expectation was that DKDP crystals between 3.5 mm and 5.5 mm would be needed to compensate the thermal lensing in the TGG crystals. However, the absorption in the newly purchased TGG crystals was lower than expected and even our shortest crystals over-



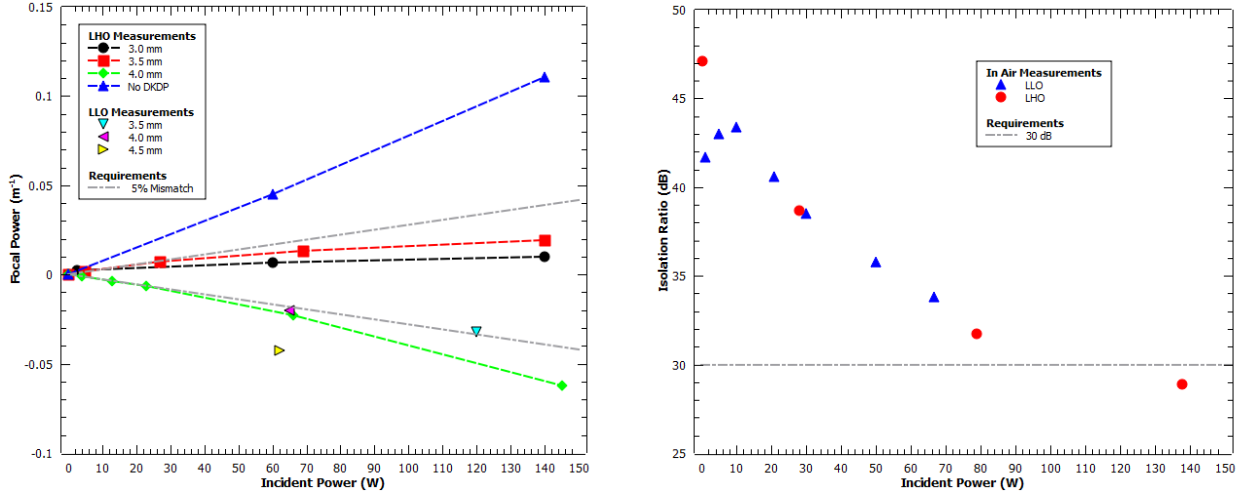


Figure 8. Left graph: Thermal lens for various DKDP crystals measured in-air as a function of laser power. Right graph: Isolation ratio measured in-air at both sites. The power is the injected power while the power inside the FI is twice as high. Therefore 70 W incident power corresponds to  $\sim 125$  W injected power during science mode when the near impedance matched interferometer reflects less than 10% of the light.

compensated. While the low absorption in TGG is obviously good, it required to shorten the originally ordered DKDP. We choose 3.5 mm for both isolators instead of the more optimum 3 mm because of concerns that a thinner DKDP crystal might fracture inside the vacuum chamber under thermal stress. Both isolators meet the thermal lensing requirements for aLIGO.

The isolation ratio was also measured as a function of input power. To do so the transmitted beam was reflected back under a negligibly small angle to allow to separate the return beam from the incoming beam. The powers in the beam going into and through the FI, and in the return beams in both polarizations were measured to determine and optimize the optical efficiency and the isolation ratio as a function of laser power. The results for both FI are shown in Figure 8. For these measurements, the power inside the FI is twice the incident power. 70 W incident power or  $\sim 140$  W inside the FI is more than the maximum power we expect during science mode when 125 W are submitted to the near impedance matched main interferometer and less than 10 W are reflected. These results show that the in-air tested FI meet the aLIGO requirements.

One problem with this approach of optimizing the isolation ratio before installation into the vacuum system is that the temperature dependence of the Verdet constant will cause the rotation of the two TGG crystals to shift after installation. This effect also causes a power dependent shift in the rotation angle. The motorized rotation stage allows to adjust the half-wave plate to compensate for these changes

and to optimize the isolation ratio in-situ for the injected power. This in-situ optimization is important because it is planned to operate aLIGO with  $\sim 20$  W of injected power during the first science runs.

Historically, the FI has always been one of the main sources of optical losses. The aLIGO FI consists of seven optical elements with a total of fourteen optical surfaces each contributing to the losses. The TGG crystals and the DKDP crystals are also known for absorbing a non-negligible fraction of the light, hence the thermal lensing (which also reduces the power in the fundamental mode). The next culprit is the polarization rotation between the two polarizers. Ideally, the FI would have  $0^\circ$  in the forward and  $90^\circ$  rotation in the backward direction. This is only possible when the TGG crystals provide exactly  $45^\circ$  in both directions and the quartz rotator and the half-wave plate combined give exactly  $\mp 45^\circ$  in the forward and backward direction, respectively. Only the isolation ratio or the optical efficiency can be optimized in-situ by rotating the half-wave plate to compensate the aforementioned changes in the Verdet constant when moving from low to high power and from air to vacuum. The measured optical efficiency of the FI was  $96.7\%$  ( $\pm 0.4\%$ ) for up to 70 W input power at LLO and  $97.7\%$  ( $\pm 0.4\%$ ) for up to 140 W at LHO.

Prior to installation of the LLO FI, the half-wave plate was temporarily adjusted to maximize the optical efficiency rather than the isolation ratio. By measuring the residual power dumped in transmission of the FI an upper limit was placed on the homogeneity of the polarization rotation at 36 ppm.

Measuring the isolation ratio in this configuration also allows for a measurement of the missing rotation in the Faraday rotator which came out to be  $\sim 1.6^\circ$  at LLO.

### C. Input Mode Cleaner

The input mode cleaner (IMC) is a resonant triangular cavity consisting of the three mirrors MC1, MC2, and MC3 which form an isosceles triangle as shown in Figure 4. The purpose of the IMC within the input optics is multifaceted. It suppresses spatial non-uniformities of the input laser beam while transmitting the diffraction limited Gaussian mode. It passively suppresses frequency and pointing noise and serves as a reference for additional active suppression. In addition, the IMC filters the polarization of the input beam before being sent to the FI. The input and output coupler (MC1 and MC3 respectively) of the IMC are nominally flat with a transmissivity of 6000 ppm while the apex mirror (MC2) has a nominal radius of curvature of 27.27 m and a transmissivity of 5 ppm. MC1 and MC3 are separated by 46.5 cm while the distance between MC2 and MC1/MC3 is 16.24 m. This gives the IMC a free spectral range of 9.099 MHz, a finesse of 515, and a cavity pole of 8.72 kHz.

The reflected beam from the IMC is brought out-of-vacuum to the IOT2L table where it is detected with a narrowband photodetector for length sensing via the Pound-Drever-Hall<sup>27</sup> (PDH) technique. Some of the reflected beam is picked off and sent to two wavefront sensors<sup>28,29</sup>, separated by  $90^\circ$  of Gouy phase, for angular sensing of the IMC. The light leaking through MC2 is sent to an in-vacuum quadrant detector for additional angular information. In addition, a sample of the transmitted light of the IMC is brought out-of-vacuum to the IOT2L table for diagnostics.

The three mirrors of the IMC are made of fused silica and have a mass of 2.9 kg. They hang from the aLIGO small triple suspensions<sup>30</sup> which provide isolation from seismic noise proportional to  $f^{-6}$  above the three resonant frequencies near 1 Hz for all degrees of freedom except vertical and roll. The vertical and roll degrees of freedom are isolated with blade springs which provide isolation proportional to  $f^{-4}$  above the two blade spring resonances near 1 Hz. Each stage of the suspensions, including the mirror, have small permanent magnets attached which can be actuated upon with electromagnets attached to the suspension frame, known as OSEMs.<sup>31,32</sup> The OSEMs also incorporate shadow sensors which use the magnets as flags to sense the important degrees of freedom of each stage. The actuation strength

gets progressively stronger at higher stages with the middle and upper stages having, respectively, an actuation authority at DC that is  $\sim 20$  times and  $\sim 1500$  times that of the mirror. Staging the actuation strength in this way prevents the applied force from spoiling the seismic isolation provided by the suspension.

Length sensing of the IMC is accomplished with the PDH technique by adding a 24.0 MHz sideband to the beam via the EOM and sensing the amplitude modulation induced when the cavity is off resonance. This signal provides an accurate comparison between the round trip length of the IMC and the frequency of the laser which is used to quiet the laser frequency above  $\sim 15$  Hz and to quiet the cavity length below  $\sim 15$  Hz. Controlling the cavity length employs hierarchical control in which control at lower frequencies is offloaded to the higher stages of the suspension. The mirror stage is offloaded to the upper stages at frequencies below  $\sim 7$  Hz, and the middle stage is offloaded to the top at frequencies below  $\sim 100$  mHz.

Angular sensing of the relative alignment between the input beam and the IMC is achieved with differential wavefront sensing,<sup>28,29</sup> a variant of the PDH technique. This technique provides independent error signals for all four relative degrees of freedom and is used to force the cavity to follow the input beam with a bandwidth of  $\sim 500$  mHz. In addition, the quadrant detector behind MC2 is used to servo two degrees of freedom of the input beam with a bandwidth of  $\sim 10$  mHz.

### D. Auxiliary mirror suspensions

The HAM Auxiliary Suspensions (HAUXes), depicted in Figure 9, are single pendulum suspensions with the addition of blade springs for vertical isolation. The main structure, made of aluminum, fits in an envelope of 127x217x441 mm (DxWxH), weighs approximately 6 kg and consists of a base, two side walls, two horizontal bars supporting four A-OSEMs (a particular variation of the sensors/actuators described in the previous section), a stiffening slab connecting the two walls and a top part supporting the blade springs. The structure is designed and tested to have the lowest structural resonance above 150 Hz, so as not to interfere with the delicate control loops of the LIGO seismic isolation platform on which it is installed.

Two 250 mm long, 150  $\mu$ m diameter steel music wires run from the tips of two 77 mm long, 500  $\mu$ m thick tapered maraging steel blades down to a lightweight circular aluminum holder containing the optic. The resonant frequencies of the op-

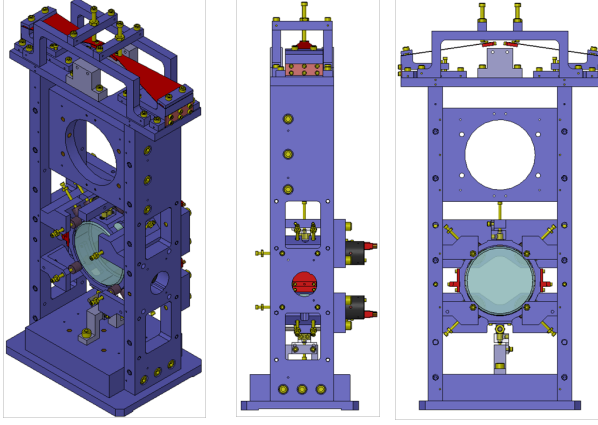


Figure 9. The HAMAux suspensions are used for the steering mirrors between the mode cleaner and the main interferometer. These are single stage suspensions with blades for vertical isolation.

tic's displacement and rotational degrees of freedom are all designed to be below 10 Hz which keeps them below the aLIGO measurement band. This is particularly important for the degrees of freedom that directly couple into beam motion; length, pitch, and yaw. According to a numerical model, the pendulum motion around the top suspension point (where the wires leave the blades) and the optic pitch motion around the lowest suspension points (where the wires attach to the optic holder) combine in two normal modes with frequencies just above and below 1 Hz. The same model shows that the yaw motion around the vertical axis has a slightly lower resonance at about 0.8 Hz.

The use of an optic holder allows for easy swapping of the optic and for the use of passive eddy current damping, while providing support for a balancing threaded rod, to fine tune the optic's pitch, and for the magnets of the four A-OSEMs, without the need of gluing them directly to the optic. The A-OSEMs are arranged in a square pattern thus providing readout and actuation capabilities for the yaw, pitch and piston degrees of freedom. The A-OSEMs are used for both beam pointing and local active damping. Passive eddy current damping along the other degrees of freedom is provided by two pairs of anti-parallel neodymium magnets attached to the main structure immediately above and below the optic holder; their distance from the holder can be changed to tune the damping action. A set of fourteen soft-tip stoppers protrude from the main structure towards the optic holder and can be used to mechanically limit the motion of the optic as well as to securely clamp it during handling and transportation of the suspensions.

The HAUXs were assembled on site and charac-

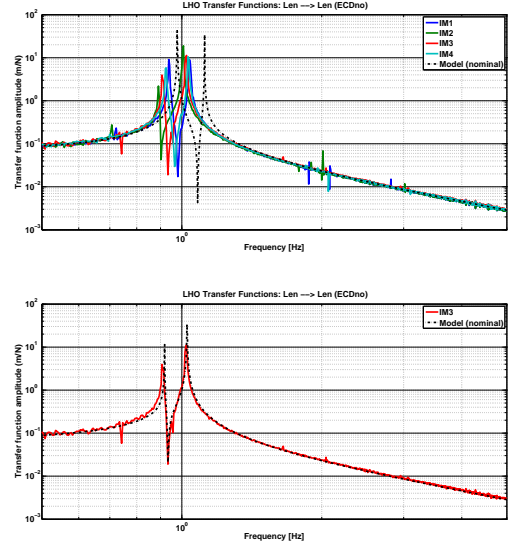


Figure 10. Top: the length-to-length transfer functions measured for four HAMAux suspensions, plotted together with the prediction from a numerical model. The differences between nominally identical suspensions are compatible with machining and assembly tolerances. The overall shift of all the measured resonance peaks towards lower frequencies compared to the model is explainable with inaccuracies in some of the parameters used in the model. Bottom: measured and modeled TF can be made to agree very well with realistic variations of the model parameters from their nominal value. Here, the model was specifically fine tuned to match the TF measured on IM3.

terized prior to installation by acquiring a complete set of transfer functions (TFs) from force (torque) applied to the optic to displacement (rotation) of the optic. For this measurement the A-OSEMs were used as both actuators and sensors. It is worth noting that, although the role of the suspension is to isolate the mirror from motion of the ground, measurement of TFs from force at the optic to displacement allows to predict the performance of the suspensions.

TFs were acquired both before and after installation of eddy current dampers, with the former providing a better tool to verify overall performance of the suspensions, since the dampers broaden the peaks and make it difficult to recognize critical features in the TFs. Figure 10 shows one example of such a TF (in this case, force versus displacement along the beam axis) measured for the 4 different suspensions assembled at LHO, as well as the value calculated from the numerical model of the suspensions.

The variability between measured transfer functions, particularly the position of the resonance

peaks, of nominally identical suspensions is well within what can be explained by machining and assembly tolerances. Since they are of little consequence, no mechanism has been incorporated in the HAUX design to allow for post-assembly compensation of these errors and fine tuning of the resonances.

Of a different nature is the systematic shift of the resonant frequencies of all measured TFs (including the ones not shown here) towards lower values compared to those predicted. It is possible to explain the observed discrepancy by assuming that the actual value of some of the parameters used in the numerical model, e.g. material properties or quantities estimated from the CAD drawing, is different from the nominal one. Unfortunately, this procedure yields multiple possible combinations of realistic parameter values; the result obtained from one particular choice of parameters is shown in the bottom of Figure 10. Identifying the correct value of the parameters would have required a long dedicated measurement campaign; given the time constraints imposed by the aLIGO installation schedule and the fact that a shift of resonances towards lower frequencies is actually an advantage, this was deemed unnecessary.

Regardless of the previous two observations, the transfer functions show the expected overall behavior and isolation in the measurement band, and the resonances are all below 10 Hz; the latter is true also for the degrees of freedom that are not nominally sensed by the A-OSEMs, but whose resonances are nevertheless detectable because of cross couplings into the A-OSEMs readout. The HAM Auxiliary Suspensions thus satisfy the design requirements.

The complete sets of transfer functions to length, pitch and yaw as well as the cross couplings have been measured for all HAUXs and are documented under LIGO document number T1300030.<sup>33</sup> All design drawings, materials, assembly instructions, and test protocols and many other documents related to the HAUX suspensions are available under LIGO document number T1300020.<sup>34</sup>

#### E. Mode matching from the PSL to the main interferometer

In order to couple the maximum amount of light from the PSL into the interferometer, it is important that the spatial mode of the laser beam be properly matched to the spatial mode of the resonant interferometers downstream. The input optics is responsible for matching the mode from the PSL into the IMC as well as matching the mode from the IMC into the interferometer. In both cases Galilean telescopes are used to avoid tightly focused beams and shorten the

telescope lengths.

The mode coming from the PSL is defined by the pre-mode cleaner (PMC, Figure 1) which has a waist size of 550  $\mu\text{m}$ . This is mode matched to the IMC by a pair of 50 mm diameter lenses rigidly mounted on the PSL table between the EOM and the power control stage. The first lens has a focal length of  $-459.5$  mm, the second lens has a focal length of  $+1145.6$  mm, the separation between the two is 838 mm, and the first lens is placed 890 mm from the PMC waist. The total distance from the PMC waist to the HR surface of MC1 is roughly 10.9 m. The IMC mode has a waist located midway between MC1 and MC3 (Figure 4) with a size of 2.12 mm. The spatial mode of the IMC is mode matched to the main interferometer by the suspended mirrors IM2 and IM3 (Figure 4) which sit before and after the FI respectively. The focal length of IM2 is 12.8 m, the focal length of IM3 is  $-6.24$  m, and the separation between them is 1.170 m. IM2 is located 1.78 m downstream of the HR surface of MC3, and the total distance from the HR surface of MC3 to that of PRM (Figure 2) is 4.59 m.

A detailed as-built layout (to scale) of the PSL table, including the relevant components of the input optics can be found at LIGO document number D1300347<sup>35</sup> for LLO and D1300348<sup>36</sup> for LHO. The coordinates of all in-vacuum optics can be found in the master coordinate list under LIGO document number E1200274<sup>37</sup> for LLO and E1200616<sup>38</sup> for LHO.

## V. PERFORMANCE OF INPUT OPTICS

This section discusses the integrated tests performed on the input optics after everything was installed into the vacuum system. Although the output power of the PSL is capable of reaching 180 W, LIGO has chosen for technical reasons to operate at powers below 30 W for the foreseeable future. This limitation prevented extended, in-vacuum tests of the FI and IMC at the high powers for which they were designed.

*Power Budget* A power budget of the input optics (IO) was made at both sites using a calibrated power meter to measure optical powers at various points throughout the system. Optical power at various key points in the vacuum system was inferred from this data by using the expected transmissivities of the pickoff mirrors, and power coupling between these key points was inferred from this data. Table I shows the calculated power coupling between the various key points of the IO for LLO (results are similar for LHO). Note that the overall IO efficiency of 84.5 % does not include the mode mismatch

Path	Power Coupling (%)
PSL to MC1	$95.3 \pm 1.3$
IMC visibility	$98.4 \pm 0.1$
IMC transmissivity	$92.2 \pm 3.1$
MC3 to PRM	$97.9 \pm 2.9$
Full IO: PSL to PRM	$84.5 \pm 2.5$

Table I. The power coupling between various points in the input optics. The overall transmissivity of the IO does not include mode matching losses into the main interferometer.

into the interferometer. Measurement of the mode mismatch is complicated since it competes with the mode matching between the power recycling cavity and the arm cavities as well as the impedance of the interferometer which, in turn, depends on knowing the precise reflectivity of all of the mirrors. The reflected light from the interferometer when it is held on resonance sets an upper limit on the mode mismatch of  $\sim 9\%$ .

*In-vacuum FI Isolation Ratio:* The in-vacuum isolation performance of the FI was measured at low power. The measurement was made by placing a pair of matched beamsplitters into the laser beam on the PSL table between lenses L1 and L2 (see Figure 3), each having a reflectivity of 32 %, and a photodiode was added to the backwards propagating beam from the IFO. With the IMC locked, the angle of PRM was adjusted in order to maximize the power on the PD. Taking into account the losses from mode matching to the IMC and the reflectivity of PRM, an isolation ratio of 29.1 dB was measured at LLO and 35.0 dB at LHO. Note that the HWP angle inside the FI was not adjusted to optimize the isolation ratio. The measured isolation ratios appear to be sufficient and rotating the HWP in situ was seen as an unnecessary risk.

*IMC Cavity Pole:* The IMC, like all optical cavities, acts as a low pass filter to variations in both laser frequency and intensity. The  $-3$  dB point of this low pass filter, the so called cavity pole, is a function of the reflectivity of the mirrors as well as the round-trip losses;

$$\Omega_0 = \frac{c}{L} \frac{1 - r^2 \sqrt{1 - \frac{\ell}{r^2}}}{r^2 \sqrt{1 - \frac{\ell}{r^2}}}, \quad (1)$$

where  $r$  is the amplitude reflectivity of MC1 and MC3 (assumed equal) and  $\ell$  is the round-trip loss.

The cavity pole of the IMC was measured by amplitude modulating the input beam and taking the transfer function between an RFPD before the IMC

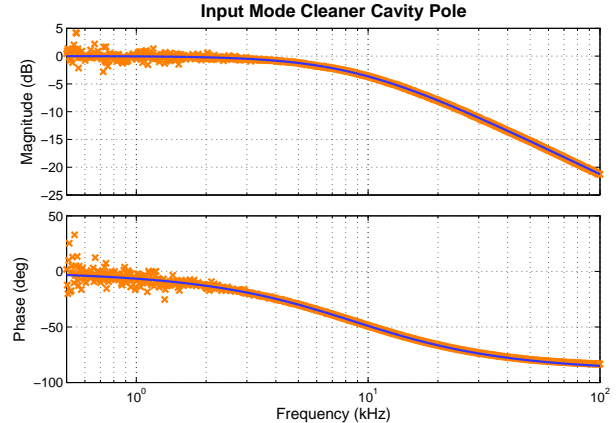


Figure 11. The measured IMC cavity pole is shown together with a simple single pole fit.

and another RFPD after the IMC. Figure 11 shows the data taken at LLO together with a single pole fit to the data. The fit has a pole frequency of  $8,686 \pm 108$  Hz which gives an IMC finesse of 522. Using the vendor measured transmissivity of MC1 and MC3, this gives a round-trip loss via (1) of  $\ell = 164 \pm 147$  ppm.

*IMC Scattering:* Scattering from the IMC mirrors was measured in-situ at LLO using calibrated digital (GigE) cameras. The available views of the optics were restricted by the vacuum system to five different locations which gives seven different views of the three optics. The extra two views are due to the fact that the scattering from MC1 and MC3 can be seen in the reflection of each other for angles near the beam line. The cameras were calibrated with an  $1.064 \mu\text{m}$  laser source for various optical powers and camera exposure/gain settings.

The surface roughness of the IMC mirrors is required to have an RMS deviation below 0.1 nm. This puts the mirrors of the IMC into the smooth surface regime in which the fluctuations of the surface height are significantly less than the wavelength of the light. This regime of optical scattering is governed by the Rayleigh-Rice theory<sup>39</sup> in which the angular distribution of the scattered light is governed solely by the statistical properties of the surface height fluctuations.<sup>40</sup> In particular, the angular distribution of the scattered light is determined by a simple mapping from the two-dimensional power spectral density of the surface height variations. Each spatial wavelength can be thought of as a diffraction grating which contributes to the scattering at the first order deflection given by

$$\sin \theta_s = \sin \theta_i \pm \frac{\lambda}{d}, \quad (2)$$

where  $d$  is the spatial wavelength of interest.



Optic	$\theta_i$ (deg)	$\theta_s$ (deg)	BRDF ( $\frac{10^{-6}}{\text{sr}}$ )	$d$ ( $\mu\text{m}$ )
MC1	44.6	45.9	$153 \pm 5$	66.6
MC1	44.6	22.5	$0.5 \pm 0.1$	3.3
MC1	44.6	-42.8	$0.025 \pm 0.001$	0.8
MC2	0.8	2.0	$5569 \pm 71$	50.8
MC2	0.8	61.2	$8.9 \pm 1.9$	1.2
MC3	44.6	45.9	$95.7 \pm 4.6$	66.6
MC3	44.6	-42.8	$0.102 \pm 0.002$	0.8

Table II. The scattering results for the three mirrors of the input mode cleaner. The incident and scattering angles, measured with respect to the optic normal are shown together with the measured BRDF and the spatial wavelength which leads to diffraction at the scattering angle.

Table II shows the results of these scatter measurements. The angle of incidence, determined by the IMC geometry, and the angle of scattering, determined by the available view of the optic, taken with respect to the optic normal, are shown in the first two columns of the table. The second two columns show the measured bi-directional reflectance distribution function (BRDF) and the spatial wavelength of the surface deformations which lead to scattering at that angle within the Rayleigh-Rice formalism. While the surface scatter of MC1 and MC3 are roughly as expected, the surface scatter of MC2 is high by more than an order of magnitude.

An estimate of the total integrated scatter (TIS) was made for all three optics by first fitting the measured data to the function  $A/(\theta_s - \theta_i)^2$ , where  $A$  is the fitting parameter. This function is empirically motivated and is typical of surface scattering seen from high quality laser line optics.<sup>41,42</sup> Integrating this function over azimuthal angles from  $\pi/2$  down to the beam divergence angle gives an estimate of the total scatter of light out of the beam. Doing so gives TIS values of 3.8 ppm for MC1, 90.2 ppm for MC2, and 5.7 ppm for MC3.

*IMC Absorption:* The total absorption of the mirrors in the IMC at LLO was measured by tracking the frequency of the resonance of the TEM<sub>01</sub> mode while the circulating power was intermittently increased and decreased. For an ideal cavity with spherical mirrors, the round-trip Gouy phase of the cavity is determined entirely by the radii of curvature of the mirrors and the distances between them. The location of the TEM<sub>01</sub> resonance is determined by this round-trip Gouy phase, and measurement of its location therefore provides a precise method for measuring changes in the radii of curvature of the mirrors. To first order a mirror which is heated by

optical absorption deforms spherically<sup>43</sup>. Tracking of the location of this resonance while modulating the power therefore provides a method of measuring the absorption of the mirrors.

The location of the TEM<sub>01</sub> resonance was measured by driving the EOM with the RF output of a network analyzer, adding phase sidebands to the carrier beam which was held on resonance by the control system of the IMC. The signal of an RF photodiode in transmission of the IMC was demodulated by the network analyzer so that, when the frequency swept across the TEM<sub>01</sub> resonance, the beating between the sideband and the carrier mapped out the resonance of the first order mode. In addition, offsets were inserted into the IMC angular control loops in order to keep it slightly misaligned and enhance the relative TEM<sub>01</sub> content of the sideband, and a small portion of the transmitted beam was occluded before being sent to the RFPD to enhance the beat signal between the fundamental mode of the carrier and the TEM<sub>01</sub> mode of the sideband. This setup was used to monitor the location of the first order resonance of the IMC while the input power was intermittently increased and decreased. Further information about the details of this technique can be found in Reference 44.

Table III shows the results of several repetitions of this measurement at LLO over the course of nearly one and a half years. The second column shows the two power levels which were used for each measurement, the third column shows the measured frequencies at those power levels, and the fourth column shows the shift in the frequencies. The last column shows the amount of inferred absorption per mirror based on a numerical model developed using a finite element simulation to calculate the thermal deformation and an FFT based beam propagation simulation to calculate the shift of the resonance. Although the absorption is slightly higher than was anticipated, the amount of inferred thermal lensing from absorption at this level only leads to a 0.3 % reduction in power coupled into the interferometer.

*IMC Length* The same setup used to measure the IMC absorption was also employed to measure the length of the IMC. By adding a small offset to the error point of the control loops which hold the IMC on resonance, the phase modulation (PM) impressed by the network analyzer via the EOM gets converted to amplitude modulation (AM) on either side of the cavity's free spectral range. Precisely on resonance the magnitude of this PM to AM conversion goes through a minimum, and the phase flips sign. Note that this is the same effect on which the Pound-Drever-Hall technique for cavity locking is based<sup>27</sup>. By scanning the sidebands across successive free spectral ranges the length of the IMC was

Date	Power (W)	$f_{01}$ (Hz)	$\Delta f_{01}$ (Hz)	Abs. (ppm/mir.)
1/17/2013	3.11	$29,266,891 \pm 60$	$6,230 \pm 69$	$2.39 \pm 0.02$
	30.5	$29,273,121 \pm 35$		
7/23/2013	0.517	$29,268,352 \pm 65$	$245 \pm 85$	$1.50 \pm 0.46$
	1.034	$29,268,597 \pm 56$		
8/6/2013	0.203	$29,267,831 \pm 14$	$358 \pm 15$	$1.42 \pm 0.06$
	1.011	$29,268,189 \pm 6.4$		
9/30/2013	1.074	$29,266,056 \pm 39$	$1,175 \pm 54$	$1.53 \pm 0.06$
	3.076	$29,267,230 \pm 37$		
6/17/2014	1.79	$29,877,736 \pm 46$	$2,249 \pm 79$	$0.50 \pm 0.01$
	10.24	$29,875,487 \pm 64$		

Table III. The data and inferred absorption from numerous repetitions of the Gouy phase absorption measurements in the IMC. The Power and  $f_{01}$  columns show the input power level and location of the TEM<sub>01</sub> peak while the  $\Delta f_{01}$  and Abs. columns show the shift in this peak between power levels and the inferred absorption.

measured at LLO to be  $32,947.3 \pm 0.1$  mm and at LHO to be  $32,946.6 \pm 0.1$  mm

*IMC Noise Budget:* As with all lock-in experiments, the feedback signals to the length and frequency paths of the IMC control system are a measure of the fluctuations in these quantities. Understanding the source of these fluctuations is important because some noise sources will be suppressed either actively or passively while others, e.g. sensing noises, can be impressed by the control system and inject noise into the main interferometer.

The noise budget for the IMC is shown in Figure 12. The red and orange curves show the feedback signals to the length and frequency respectively, and the dashed gray line shows the coherent sum of these two. The other curves on the plot are a mixture of measured noise and theoretical predictions propagated to the error point with a controls model. At low frequencies, below  $\sim 5$  Hz, the dominant sources of noise are from seismic motion of the mirror suspensions and sensor noise injected through the active control loops. At high frequencies, above  $\sim 80$  Hz, the dominant noise is caused by frequency noise of the incident laser beam which is created, at least in part, by vibrations of the injection bench on which the PSL is built (see yellow and orange trace in Figure 12).

The missing noise between 5 Hz and 80 Hz was the subject of many investigations, but is still not fully understood. The level of the noise in this region averages around that shown in Figure 12 but fluctuates on day timescales by as much as an order of magnitude but never coming down to the level of the understood noise.

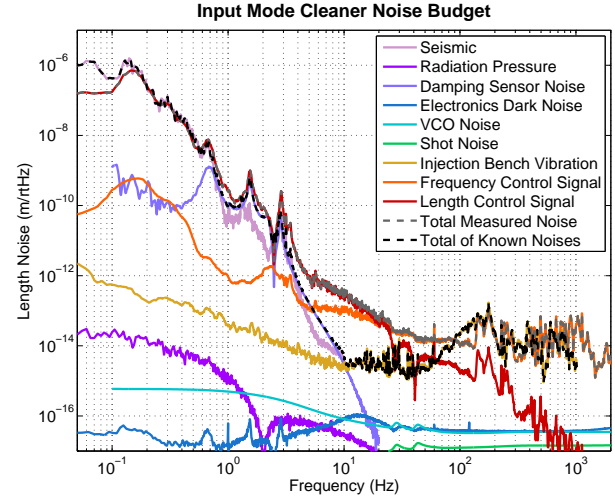


Figure 12. The noise budget of the aLIGO input mode cleaner. The measured noise in the length path is shown in red, the measured noise of the frequency path is shown in orange, and the sum total of these two is shown in dashed gray. The sum total of the understood noises is shown in dashed black, and the individual terms are discussed in the text.

## VI. OUTLOOK AND CONCLUSIONS

In summary, we have presented the design of the major components of the aLIGO input optics in full detail. Our EOM is capable of simultaneously adding three RF sidebands with minimal thermal lensing at CW powers of up to 200 W all while maintaining an RFAM level below  $10^{-4}$ . Our FI design provides greater than 30 dB of isolation at CW powers of up to 200 W (single pass) with relatively small

thermal lensing. The input mode cleaner uses mirrors hanging from the aLIGO triple suspensions to provide sensing limited length noise fluctuations of  $\sim 1 \frac{\text{fm}}{\sqrt{\text{Hz}}}$  above 10 Hz while transmitting 165 W of CW laser power. Finally, the HAM auxiliary suspensions isolate the laser beam from seismic fluctuations above their pole frequencies near 1 Hz while allowing for active control of the pointing of the laser beam into the interferometer.

We also presented a comprehensive set of tests of the full integrated input optics system which showed that the individual components of the input optics continue to function well when integrated into the aLIGO interferometers. We showed that the full integrated system is capable of delivering 84.5 % of the incident power to the input of the main interferometer. We showed that the FI provide greater than 29 dB of isolation at low power, a value which is expected to rise once the half-wave plate has been optimized. The scattered light from the optics of the IMC was measured and found to be below 6 ppm except for one mirror whose scattering is expected to come down with a subsequent cleaning. The absorption of the IMC was also measured to be consistently below 5 ppm per mirror over the course of nearly one and a half years. A noise budget for the IMC was presented which showed that the IMC is frequency noise limited above 100 Hz and can therefore serve as an reference for active control of the incident laser frequency variations.

## REFERENCES

- <sup>1</sup>P. Kwee, C. Bogan, K. Danzmann, M. Frede, H. Kim, P. King, J. Pödl, O. Puncken, R. L. Savage, and F. Seifert, "Stabilized high-power laser system for the gravitational wave detector advanced LIGO," *Optics express* **20**, 10617–10634 (2012).
- <sup>2</sup>G. M. Harry and the LIGO Scientific Collaboration, "Advanced LIGO: the next generation of gravitational wave detectors," *Classical and Quantum Gravity* **27**, 084006 (2010).
- <sup>3</sup>B. J. Meers, "Recycling in laser-interferometric gravitational-wave detectors," *Physical Review D* **38**, 2317 (1988).
- <sup>4</sup>J. Mizuno, K. A. Strain, P. G. Nelson, J. M. Chen, R. Schilling, A. Rüdiger, W. Winkler, and K. Danzmann, "Resonant sideband extraction: a new configuration for interferometric gravitational wave detectors," *Physics Letters A* **175**, 273–276 (1993).
- <sup>5</sup>A. J. Mullavey, B. J. Slagmolen, J. Miller, M. Evans, P. Fritschel, D. Sigg, S. J. Waldman, D. A. Shaddock, and D. E. McClelland, "Arm-length stabilisation for interferometric gravitational-wave detectors using frequency-doubled auxiliary lasers," *Optics express* **20**, 81–89 (2012).
- <sup>6</sup>HAM: Horizontal Access Modules are nearly spherical vacuum chambers with a diameter of about 2.8 m.
- <sup>7</sup>IOT2R: Input Optics Table on the Right side of HAM2.
- <sup>8</sup>The LIGO Document Control Center (DCC) is an on line repository of documents produced by members of LIGO and the LIGO Scientific Collaboration. It is accessible from any modern web browser at the url <https://dcc.ligo.org>.
- <sup>9</sup>G. C. Ciani, D. Feldbaum, J. Gleason, M. Heintze, R. M. Martin, G. Mueller, C. L. Mueller, D. B. Tanner, and L. Williams, "aLIGO input optics acceptance documentation," LIGO Document Control Center , E1201013 (2012).
- <sup>10</sup>R. Abbott, R. X. Adhikari, S. W. Ballmer, L. Barsotti, M. Evans, P. Fritschel, V. V. Frolov, G. Mueller, B. J. J. Slagmolen, and S. J. Waldman, "Advanced LIGO length sensing and control final design," LIGO Document Control Center , T1000298 (2010).
- <sup>11</sup>T. T. Fricke, N. D. Smith-Lefebvre, R. Abbott, R. Adhikari, K. L. Dooley, M. Evans, P. Fritschel, V. V. Frolov, K. Kawabe, J. S. Kissel, B. J. J. Slagmolen, and S. J. Waldman, "DC readout experiment in enhanced LIGO," *Classical and Quantum Gravity* **29**, 065005 (2012).
- <sup>12</sup>C. Krämer, "Function and interface document of inner aLIGO PSL power stabilization," LIGO Document Control Center , T0900630 (2010).
- <sup>13</sup>K. Kokeyama, K. Izumi, W. Z. Korth, N. Smith-Lefebvre, K. Arai, and R. X. Adhikari, "Residual amplitude modulation in interferometric gravitational wave detectors," *Journal of the Optical Society of America A* **31**, 81 (2014).
- <sup>14</sup>G. Mueller, "Beam jitter coupling in advanced LIGO," *Optics express* **13**, 7118–7132 (2005).
- <sup>15</sup>F. Acernese et. al., "Results of the virgo central interferometer commissioning," *Classical and Quantum Gravity* **21**, S395 (2004).
- <sup>16</sup>M. A. Arain, G. Mueller, R. M. Martin, V. Quetschke, D. H. Reitze, D. B. Tanner, and L. Williams, "Input optics subsystem design requirements document," LIGO Document Control Center , T020020 (2009).
- <sup>17</sup>University of Florida Input Optics Group, "Upgrading the input optics for high power operation," LIGO Document Control Center , T060267 (2006).
- <sup>18</sup>H. Albrecht, P. Villeval, and C. Bonnin, "Study of RTP crystal used as electro-optic modulator," in *Advanced Solid-State Photonics* (Optical Society of America, 2006) p. MB3.
- <sup>19</sup>K. L. Dooley, M. A. Arain, D. Feldbaum, V. V. Frolov, M. Heintze, D. Hoak, E. A. Khazanov, A. Lucianetti, R. M. Martin, and G. Mueller, "Thermal effects in the input optics of the enhanced laser interferometer gravitational-wave observatory interferometers," *Review of Scientific Instruments* **83** (2012).
- <sup>20</sup>V. Quetschke, W. Wu, L. Williams, M. Arain, R. Martin, D. Reitze, D. Tanner, and G. Mueller, "Method and apparatus for modulating light," (2013), US Patent 8,446,657.
- <sup>21</sup>V. Quetschke, J. Gleason, L. Williams, R. M. Martin, and G. Mueller, "Input optics acceptance documentation: Eom electro-optic modulator," LIGO Document Control Center , T1300084 (2013).
- <sup>22</sup>I. Snetkov, I. Mukhin, O. Palashov, and E. Khazanov, "Compensation of thermally induced depolarization in faraday isolators for high average power lasers," *Optics express* **19**, 6366–6376 (2011).
- <sup>23</sup>E. Khazanov, N. Andreev, A. Mal'shakov, O. Palashov, A. Poteomkin, A. Sergeev, A. Shaykin, V. Zelenogorsky, I. Ivanov, R. Amin, G. Mueller, D. Tanner, and D. Reitze, "Compensation of thermally induced modal distortions in faraday isolators," *IEEE Journal of Quantum Electronics* **40**, 1500–1510 (2004).
- <sup>24</sup>E. Khazanov, N. Andreev, A. Babin, A. Kiselev, O. Palashov, and D. H. Reitze, "Suppression of self-induced depolarization of high-power laser radiation in glass-based faraday isolators," *JOSA B* **17**, 99–102 (2000).
- <sup>25</sup>K. Shiraishi, F. Tajima, and S. Kawakami, "Compact faraday rotator for an optical isolator using magnets arranged with alternating polarities," *Optics letters* **11**, 82–84 (1986).

- <sup>26</sup>O. V. Palashov, D. S. Zheleznov, A. V. Voitovich, V. V. Zelenogorsky, E. E. Kamenetsky, E. A. Khazanov, R. M. Martin, K. L. Dooley, L. Williams, and A. Lucianetti, “High-vacuum-compatible high-power faraday isolators for gravitational-wave interferometers,” *JOSA B* **29**, 1784–1792 (2012).
- <sup>27</sup>R. W. P. Drever, J. L. Hall, F. V. Kowalski, J. Hough, G. M. Ford, A. J. Munley, and H. Ward, “Laser phase and frequency stabilization using an optical resonator,” *Applied Physics B* **31**, 97–105 (1983).
- <sup>28</sup>D. Z. Anderson, “Alignment of resonant optical cavities,” *Applied Optics* **23**, 2944–2949 (1984).
- <sup>29</sup>P. Fritschel, N. Mavalvala, D. Shoemaker, D. Sigg, M. Zucker, and G. González, “Alignment of an interferometric gravitational wave detector,” *Applied Optics* **37**, 6734–6747 (1998).
- <sup>30</sup>N. A. Robertson, M. Barton, M. Meyer, J. Romie, C. Torrie, and J. Kissel, “Ham triple suspension final design document,” LIGO Document Control Center , T0900435 (2009).
- <sup>31</sup>R. Abbott, M. Barton, B. Bland, B. Moore, C. Osthelder, and J. Romie, “Advanced ligo osem final design document,” LIGO Document Control Center , T0900286 (2009).
- <sup>32</sup>L. Carbone, S. M. Aston, R. M. Cutler, A. Freise, J. Greenhalgh, J. Heefner, D. Hoyland, N. A. Lockerbie, D. Lodhia, N. A. Robertson, C. C. Speake, K. A. Strain, and A. Vecchio, “Sensors and actuators for the advanced LIGO mirror suspensions,” *Classical and Quantum Gravity* **29**, 115005 (2012).
- <sup>33</sup>G. Ciani, D. Feldbaum, J. Gleason, R. M. Martin, C. L. Mueller, G. Mueller, D. B. Tanner, and L. Williams, “Io haux installation and testing,” LIGO Document Control Center , T1300030 (2013).
- <sup>34</sup>G. Ciani, D. Feldbaum, J. Gleason, R. M. Martin, C. L. Mueller, G. Mueller, D. B. Tanner, and L. Williams, “Input optics acceptance documentation: HAM auxiliary suspension,” LIGO Document Control Center , T1300020 (2013).
- <sup>35</sup>J. Gleason and R. M. Martin, “As built PSL table layout for advanced LIGO I1,” LIGO Document Control Center , D1300347 (2013).
- <sup>36</sup>J. Gleason and R. M. Martin, “As built PSL table layout for advanced LIGO h1,” LIGO Document Control Center , D1300348 (2013).
- <sup>37</sup>L. Williams, “aLIGO IO L1 master coordinate list,” LIGO Document Control Center , E1200274 (2012).
- <sup>38</sup>L. Williams, “aLIGO IO H1 master coordinate list,” LIGO Document Control Center , E1200616 (2012).
- <sup>39</sup>S. Schröder, A. Duparré, L. Coriand, A. Tünnermann, D. H. Penalver, and J. E. Harvey, “Modeling of light scattering in different regimes of surface roughness,” *Optics express* **19**, 9820–9835 (2011).
- <sup>40</sup>E. L. Church, H. A. Jenkinson, and J. M. Zavada, “Relationship between surface scattering and microtopographic features,” *Optical Engineering* **18**, 182125–182125 (1979).
- <sup>41</sup>F. Magaña Sandoval, R. X. Adhikari, V. Frolov, J. Harms, J. Lee, S. Sankar, P. R. Saulson, and J. R. Smith, “Large-angle scattered light measurements for quantum-noise filter cavity design studies,” *JOSA A* **29**, 1722–1727 (2012).
- <sup>42</sup>D. Gloge, E. L. Chinnock, and H. E. Earl, “Scattering from dielectric mirrors,” *The Bell System Technical Journal* (1969).
- <sup>43</sup>W. Winkler, K. Danzmann, A. Rüdiger, and R. Schilling, “Heating by optical absorption and the performance of interferometric gravitational-wave detectors,” *Physical Review A* **44**, 7022–7036 (1991).
- <sup>44</sup>C. L. Mueller, P. Fulda, R. X. Adhikari, K. Arai, A. F. Brooks, R. Chakraborty, V. V. Frolov, P. Fritschel, E. J. King, D. B. Tanner, H. Yamamoto, and G. Mueller, “In-situ characterization of the thermal state of resonant optical interferometers via tracking of their higher-order mode resonances,” (2015), arXiv:1502.02284 [gr-qc].